

Design and Implementation of Multi-Axis Motion Control in Flight Simulator Systems

Ming-Yen Wei * and Wen-Hao Cai **

Keywords : Simulator System, Multi-axis Motion Control, Data Transmission, Operational Safety.

ABSTRACT

This study aims to explore a flight simulator system for multi-axis motion control, focusing on operational safety and data transmission speed. New concepts in mechanism design, multi-axis motion control, and control system design are presented. The proposed method leverages flight, servo, and motion control technologies to strengthen control protection, simulation, and responsiveness, thereby enhancing system performance. The system's effectiveness was confirmed through testing with photoelectric switches. Furthermore, a measurement system was utilized to capture dynamic characteristics such as stroke, velocity, and acceleration. The integration of multi-axis motion control, data transmission, Ethernet Control Automation Technology (EtherCAT) technology, and photoelectric switches enhances control protection and responsiveness within simulator systems. The system overview emphasizes the structural components of the cockpit and the integration of six photoelectric switches to improve data transmission speed and safety. The architecture of the multi-axis motion control system includes a motion cueing algorithm (MCA) based on digital signal processor (DSP) technology and programmable logic controller (PLC) controllers for servo motion control. The experiment demonstrates the system's response to personnel intrusion and complex motions, highlighting its safety features and effectiveness. This approach represents a valuable contribution to the field of multi-axis motion control systems, enhancing operational safety, data transmission speed, and control responsiveness.

Paper Received December, 2023. Revised July, 2024. Accepted August, 2024. Author for Correspondence: Ming-Yen Wei.

* Assistant Professor, Department of Electrical Engineering, National Formosa University, Huwei, Yunlin, Taiwan 632, ROC.

** Graduate Student, Department of Electrical Engineering, National Formosa University, Huwei, Yunlin, Taiwan 632, ROC.

INTRODUCTION

Simulator systems play a crucial role in various industries, providing realistic and cost-effective training, testing, and research environments. These systems aim to replicate real-world scenarios and offer users a simulated environment for experiential learning and skill development. Control protection, synchronization, and responsiveness are essential factors in achieving accurate and reliable performance in systems. Prochazka et al. (2021) elucidated that the wiring configuration of the control system is susceptible to noise interference, which posing challenges in ensuring robust control.

Wei et al. (2022) describe the widespread application of the Stewart platform in flight training, offering six degrees of freedom motion space. Originally developed in 1956 by Gough (1956) and further improved by Stewart (1965), the Stewart platform has been a standard in flight simulators. Over time, a number of literatures (Wang et al. (2002); Japiong et al. (2016); Wei (2021)) research on the platform has expanded, leading to its application in various fields such as multi-axis processing machines, medical surgery auxiliary platforms, and virtual motion simulators. The Stewart platform is composed of a stationary base plate and a mobile top plate, linked by six electric cylinders that have adjustable rod lengths. Bi et al. (2019) utilized the variation in rod length, measured using optical encoders, and allows the top plate to move in six degrees of freedom. For simulators, in order to generate realistic force and angular velocity effects similar to actual vehicles, control platform motors are utilized to achieve six-axis pose transformations. However, Nagata et al. (2013) exploring the traditional servo control technologies adopted in automation equipment or simulator platforms often face challenges such as slow data transmission, poor real-time performance, complex wiring, and signal interference. To address these challenges, Wang et al. (2021) the use of EtherCAT communication protocol has been widely adopted in the industry. The system architecture consists of a Master and Slaves, where the controller on the Master side can be implemented through a standard Ethernet card, and the Slave devices utilize dedicated hardware controller chips. EtherCAT offers advantages such as

simplified wiring, excellent noise resistance, and cost-effectiveness. Ferrari et al. (2009) based on the concept of distributed control, it enables integration of servos for different axes to achieve high-speed and high-precision motion control.

During flight missions, a pilot's visual observation and sense of movement provide perceptible information for appropriate responses. The pilot's vestibular system, which is impacted by gravitational changes during flight, has an influence on the pilot's vision, spatial orientation, and aircraft control. To simulate the impact on the pilot's balance system, simulators employ a wash-out algorithm. Asadi et al. (2019) by leveraging the inner ear's vestibular system, which detects linear and rotational speed and acceleration, a motion platform replicates a wide range of motion, creating realistic dynamic effects. To enhance control capabilities, an integrated motion cueing algorithm and adaptive control techniques are employed. Zhao and Duan (2019) unitized techniques improve servo synchronous tracking and adaptively estimate parameters to control the platform effectively. Other approaches, (Qazani et al. (2019); Asadi et al. (2017)) such as filter models designed through predictive control or optimization theory, are used to modify parameters and achieve optimal control. Barbara et al. (2022) studied the development of a pilot's cockpit scanning strategy and emphasized the value of gaze behavior analysis. Further research should include diverse expert groups, larger sample sizes, and novice pilots with prior flying experience. Expanding the statistical analysis of oculographic parameters enhances our understanding of visual behavior. Utilizing eye tracking in pilot training aids in identifying and improving scanning techniques. Real-time analysis in simulator conditions allows for instructor feedback, incorporating quantitative eye movement measures. Combining flight parameter analysis with eye tracking data evaluates the effectiveness of flight training. Golebiewski et al. (2022) study explores the environmental impact of using flight simulators for pilot training compared to traditional aircraft operations. The research investigates energy consumption based on different flight scenarios and simulator configurations. Results show that flight simulators have a significantly lower negative impact on the environment compared to actual flights. The utilization of a motion platform, along with varying weather conditions, has an impact on energy consumption, potentially leading to reductions of up to 50%. When compared to aircraft training, flight simulators have the potential to decrease energy consumption in pilot training by as much as 97%.

In their study, Berthoz et al. (2013) examined different motion scale factors in a driving simulator. They found that participants who received motion feedback drove with increased caution and exhibited better car control. As a result, they were able to

anticipate the dynamic behavior of the vehicle more effectively and were less startled in the event of a crash. On the other hand, a significant degradation in driving performance was observed when motion cues were greatly reduced or absent. In a separate work, Qazani et al. (2019) developed an innovative linear time-varying model predictive control (MPC)-based motion cueing algorithm (MCA) specifically designed for simulation-based motion platforms employing hexapod mechanisms. Unlike existing methods, this approach considers the parameters of the hexapod mechanism, resulting in more precise and realistic motion cues for users. The study also acknowledges the challenges of real-time implementation due to computational requirements. Simulator motion platforms have large workspaces, but reduced interdependence between kinematic chains. Teufel et al. (2007) adapted KUKA Robocoaster enables real-time motion simulation with low delay, making it suitable for flight simulation and multi-sensory research. It is important to note that while parallel platforms offer high payload and efficiency, serial devices provide greater workspace and flexibility at a higher cost. However, it should be emphasized that when using serial arm configurations, additional attention must be given to ensure adequate safety measures are in place due to the increased interdependence of the kinematic chains.

To bolster operational safety and enhance data transmission speed, the system incorporates six photoelectric switches. They also increase resistance to external disturbances and noise, ensuring strong control signals. This study introduces new concepts in mechanism design, multi-axis motion control. The proposed methodology uses flight, servo, and motion control techniques to enhance control protection, synchronization, and responsiveness, resulting in improved system performance. Intrusion testing using photoelectric switches confirms the effectiveness of the approach. The research demonstrates the system's robustness and precise control even under challenging conditions. By integrating multi-axis motion control, data transmission, EtherCAT technology, and photoelectric switches, the proposed methodology enhances control protection, synchronization, and responsiveness in simulator systems. A comprehensive human-machine interface (HMI) and thorough intrusion testing ensure precision, reliability, and safety in simulator operations. This integrated approach overcomes challenges posed by noise interference and utilizes advanced technologies to achieve accurate and responsive control in flight simulator applications.

SYSTEM ARCHITECTURE

According to **Figure 1(a)**, the cockpit consists of an inner gimbal, an outer gimbal, and an upper/lower axis slide seat, indicating three rotational axes: pitch,

roll, and yaw. The main structure is made of cast aluminum, manufactured using aluminum processing machinery and by collaborating with relevant manufacturers. The three linear axes are designed with the heave axis's travel achieved through the movement of the upper/lower axis slide seat. Therefore, the upper/lower axis slide seat is also made of cast aluminum. In addition, the surge and sway axes are made of cast iron and consist of the surge and sway base, the lateral column, and the sway axis slide seat. On the left side of the platform, a 30kVA uninterrupted power supply (UPS) system is installed to serve as an emergency temporary power source. At the rear, there is an electrical control cabinet for equipment power control and operation. **Figure 1(b)** illustrates the design drawing for the installation of six photoelectric switches. The photoelectric switches are installed in front of the main door, the boarding ladder, the cockpit door, the safety door, the front of the platform, and the rear of the platform. Through a PLC controller employing EtherCAT, the six photoelectric switches are integrated to drive the six-axis motion platform, enhancing data transmission speed, safety, and communication anti-interference capabilities of the simulator. This improvement enables effective training with long travel distances and large angular motions.

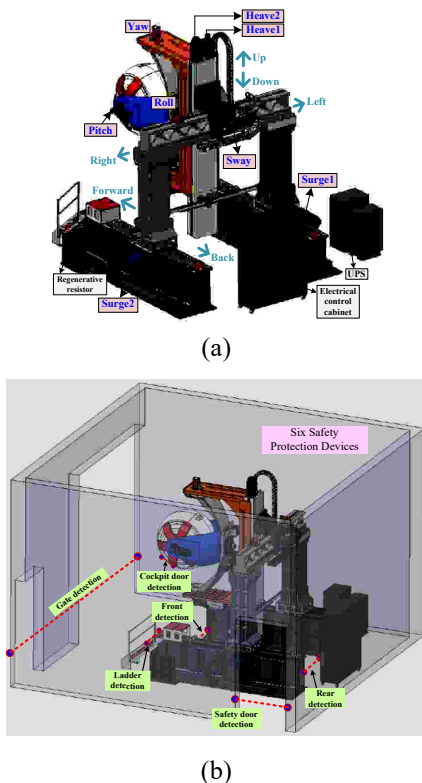


Fig. 1 The proposed multi-axis motion control simulator system: (a) 6DoF platform; (b) photoelectric switches detect objects in the installation area.

THE MULTI-AXIS MOTION

CONTROL

Wei (2022) studied the MCA in this study is designed using the DSP-based algorithm. In simulator training, the human body has a limited range within which it can perceive acceleration and speed. Movements that exceed this range can result in a delayed or less sensitive response from the human body. To provide a realistic experience for pilots during operation, Wei et al. (2022) specialized control strategies and combined with FlightGear visual effects software have been developed in simulators. These strategies are based on the unique sensory-motor model of humans and have led to the development of MCA. The MCA involves the processing of linear acceleration and angular velocity signals using filter design and processing. This, in turn, allows for the calculation of the motion state of each servo in the motion platform through kinematics. The PLC controller employs two virtual axis commands to activate the surge1 and surge2 axes, as well as the heave1 and heave2 axes, enabling them to function as real axes that track their respective virtual axes for precise motion control. Each surge and heave axis has a corresponding virtual axis with a 1ms cycle time, ensuring that surge1 and surge2, as well as heave1 and heave2, move in sync with their virtual counterparts. The control system integrates both DSP and PLC controllers to manage servo motion control effectively. The DSP handles the execution of the digital MCA at the command end and communicates data with the PLC through Ethernet. In addition to utilizing EtherCAT network communication, the PLC controller can receive relevant commands from the DSP via Ethernet. Operators can monitor and obtain real-time servo status, including axis positions, velocities, torques, and other critical information, through a 12-inch HMI display device. This setup ensures precise control and monitoring of the servo motion system, enhancing overall performance and reliability.

In **Figure 2**, the correlation between the cockpit's internal-to-external rotation is depicted, following the sequence of pitch, roll, and yaw, symbolizing the values for β , α , and γ .

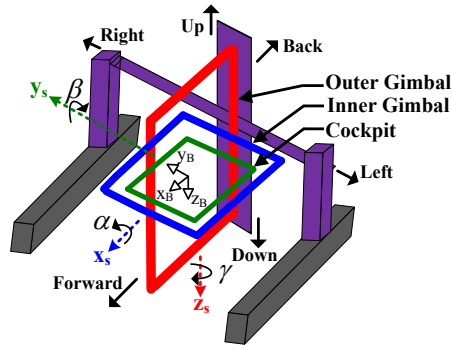


Fig. 2 Rotation correlation.

To get the coordinate transformation relation as

$$\begin{bmatrix} x_s \\ y_s \\ z_s \end{bmatrix} = \begin{bmatrix} (\cos \beta) & 0 & (\sin \beta) \\ 0 & 1 & 0 \\ -(\sin \beta) & 0 & (\cos \beta) \end{bmatrix} \begin{bmatrix} x_\sigma \\ y_\sigma \\ z_\sigma \end{bmatrix} \quad (1)$$

$$\begin{bmatrix} x_\sigma \\ y_\sigma \\ z_\sigma \end{bmatrix} = \begin{bmatrix} 1 & 0 & 0 \\ 0 & (\cos \alpha) & -(\sin \alpha) \\ 0 & (\sin \alpha) & (\cos \alpha) \end{bmatrix} \begin{bmatrix} x_\mu \\ y_\mu \\ z_\mu \end{bmatrix} \quad (2)$$

$$\begin{bmatrix} x_\mu \\ y_\mu \\ z_\mu \end{bmatrix} = \begin{bmatrix} (\cos \gamma) & -(\sin \gamma) & 0 \\ (\sin \gamma) & (\cos \gamma) & 0 \\ 0 & 0 & 1 \end{bmatrix} \begin{bmatrix} x_B \\ y_B \\ z_B \end{bmatrix} \quad (3)$$

By using the conversion relationships presented in Equations (1) to (3), we can establish the relationship between the inertial coordinate vector ψ^I and the body coordinate vector ψ^B

$$\psi^I = R_\Phi \psi^B \quad (4)$$

where R_Φ represents the rotation matrix from body coordinates to inertial coordinates, it can be expressed as follows.

$$R_\Phi = R_y R_x R_z \quad (5)$$

where R_x , R_y , and R_z represent the rotation matrices for the surge, sway, and heave axes, respectively. Substitute Equations (1) to (3) into Equation (5), we obtain

$$R_\Phi = \begin{bmatrix} \cos \beta & 0 & \sin \beta \\ 0 & 1 & 0 \\ -\sin \beta & 0 & \cos \beta \end{bmatrix} \begin{bmatrix} 1 & 0 & 0 \\ 0 & \cos \alpha & -\sin \alpha \\ 0 & \sin \alpha & \cos \alpha \end{bmatrix} \begin{bmatrix} \cos \gamma & -\sin \gamma & 0 \\ \sin \gamma & \cos \gamma & 0 \\ 0 & 0 & 1 \end{bmatrix} \quad (6)$$

$$= \begin{bmatrix} \cos \gamma \cos \beta + \sin \alpha \sin \gamma \sin \beta & \cos \gamma \sin \alpha \sin \beta - \cos \beta \sin \gamma & \cos \alpha \sin \beta \\ \cos \alpha \sin \gamma & \cos \alpha \cos \gamma & -\sin \alpha \\ \cos \beta \sin \alpha \sin \gamma - \cos \gamma \sin \beta & \sin \gamma \sin \beta + \cos \gamma \cos \beta \sin \alpha & \cos \alpha \cos \beta \end{bmatrix}$$

The transformation matrix from body coordinates to inertial coordinates, denoted as T_Φ and assumed to be represented using homogeneous coordinates, can be expressed as:

$$T_\Phi = \begin{bmatrix} \cos \gamma \cos \beta + \sin \alpha \sin \gamma \sin \beta & \cos \gamma \sin \alpha \sin \beta - \cos \beta \sin \gamma & \cos \alpha \sin \beta & x \\ \cos \alpha \sin \gamma & \cos \alpha \cos \gamma & -\sin \alpha & y \\ \cos \beta \sin \alpha \sin \gamma - \cos \gamma \sin \beta & \sin \gamma \sin \beta + \cos \gamma \cos \beta \sin \alpha & \cos \alpha \cos \beta & z \\ 0 & 0 & 0 & 1 \end{bmatrix} \quad (7)$$

$$= \begin{bmatrix} x_x & y_x & z_x & o_x \\ x_y & y_y & z_y & o_y \\ x_z & y_z & z_z & o_z \\ 0 & 0 & 0 & 1 \end{bmatrix}$$

The expression for the angular velocity of the rotation in simulator body coordinates is:

$$\vec{\omega}^B = \begin{bmatrix} p \\ q \\ r \end{bmatrix} \quad (8)$$

The expression for the angular velocity of the rotation in simulator axis coordinates is:

$$\dot{P} = \begin{bmatrix} \dot{\alpha} \\ \dot{\beta} \\ \dot{\gamma} \end{bmatrix} \quad (9)$$

By rearranging Equations (8) and (9), one can obtain:

$$p \cdot (\bar{x}_B) + q \cdot (\bar{y}_B) + r \cdot (\bar{z}_B) = \dot{\beta} \cdot (\bar{y}_\sigma) + \dot{\alpha} \cdot (\bar{x}_\mu) + \dot{\gamma} \cdot (\bar{z}_B) \quad (10)$$

Rearranging Equations (2) and (3) into Equation (10), we have the following expression:

$$\begin{aligned} \bar{y}_\sigma &= (\cos \alpha) \cdot \bar{y}_\mu - (\sin \alpha) \cdot \bar{z}_\mu \\ &= (\cos \alpha \sin \gamma) \cdot \bar{x}_B + (\cos \alpha \cos \gamma) \cdot \bar{y}_B - (\sin \alpha) \cdot \bar{z}_B \end{aligned} \quad (11)$$

By substituting Equations (3) and (11) into Equation (10), we obtain the following expression:

$$\begin{aligned} &p \cdot (\bar{x}_B) + q \cdot (\bar{y}_B) + r \cdot (\bar{z}_B) \\ &= [\dot{\beta} \cdot (\cos \alpha \cos \gamma) + \dot{\alpha} \cdot (\cos \gamma)] \bar{x}_B \\ &\quad + [\dot{\beta} \cdot (\cos \alpha \cos \gamma) - \dot{\alpha} \cdot (\sin \gamma)] \bar{y}_B \\ &\quad + [\dot{\gamma} - \dot{\beta} \cdot (\sin \alpha)] \bar{z}_B \end{aligned} \quad (12)$$

The conversion of the rotational angular velocity of the simulator axis coordinate to the rotational angular velocity of the body coordinate is given by:

$$\begin{bmatrix} p \\ q \\ r \end{bmatrix} = \begin{bmatrix} (\cos \gamma) & (\cos \alpha) \cdot (\cos \gamma) & 0 \\ -(\sin \gamma) & (\cos \alpha) \cdot (\cos \gamma) & 0 \\ 0 & -(\sin \alpha) & 1 \end{bmatrix} \begin{bmatrix} \dot{\alpha} \\ \dot{\beta} \\ \dot{\gamma} \end{bmatrix} \quad (13)$$

To calculate the required platform axis coordinates $(x, y, z, \alpha, \beta, \gamma)$, one needs to determine the position (o_x, o_y, o_z) , the attitude in the x-direction \bar{x} , the attitude in the y-direction \bar{y} , and the attitude in the z-direction \bar{z} . Thus, equation (5) can be expressed as

$$R_x R_z = R_y^{-1} R_\Phi$$

$$= \begin{bmatrix} (\cos \gamma) & -(\sin \gamma) & 0 \\ (\cos \alpha \cdot \sin \gamma) & (\cos \alpha \cdot \cos \gamma) & -(\sin \alpha) \\ (\sin \alpha \cdot \sin \gamma) & (\cos \gamma \cdot \sin \alpha) & (\cos \alpha) \end{bmatrix} \quad (14)$$

The above equation shows simplification by multiplying both sides by R_y^{-1} . By observing that Formula (7) involves the x-direction attitude \bar{x} , the y-direction attitude \bar{y} , and the z-direction attitude \bar{z} , we can express equations (6) and (7) in terms of

the following relationship:

$$\begin{aligned}
R_y^{-1}R_\alpha &= \begin{bmatrix} x_x \cdot \cos \beta - x_z \cdot \sin \beta & y_x x_x \cdot \cos \beta - y_z \cdot \sin \beta & z_x \cdot \cos \beta - z_z \cdot \sin \beta \\ x_y & y_y & z_y \\ x_x \cdot \sin \beta + x_z \cdot \cos \beta & y_x \cdot \sin \beta + y_z \cdot \cos \beta & z_x \cdot \sin \beta + z_z \cdot \cos \beta \end{bmatrix} \quad (15) \\
&= \begin{bmatrix} (\cos \gamma) & -(\sin \gamma) & 0 \\ (\cos \alpha) \cdot (\sin \gamma) & (\cos \alpha) \cdot (\cos \gamma) & -(\sin \alpha) \\ (\sin \alpha) \cdot (\sin \gamma) & (\cos \gamma) \cdot (\sin \alpha) & (\cos \alpha) \end{bmatrix}
\end{aligned}$$

Then the above formula can be expressed as

$$(z_x) \cdot (\cos \beta) - (z_z) \cdot (\sin \beta) = 0 \quad (16)$$

After rearranging, we obtain

$$\tan \beta = \left(\frac{\sin \beta}{\cos \beta} \right) = \left(\frac{z_x}{z_z} \right) \quad (17)$$

Applying the arc tangent function, we can obtain the rotation angle of the pitch axis as:

$$\beta = \tan^{-1} \left(\frac{z_x}{z_z} \right) \quad (18)$$

After obtaining the angle β from Equation (18), it can be arranged according to the relationship described in Equation (15).

$$(\sin \alpha) = -(z_y) \quad (19)$$

$$(\cos \alpha) = [(z_x) \cdot (\sin \beta) + (z_z) \cdot (\cos \beta)] \quad (20)$$

$$(\sin \gamma) = [-(y_x x_x) \cdot (\cos \beta) + (y_z) \cdot (\sin \beta)] \quad (21)$$

$$(\cos \gamma) = [(x_x) \cdot (\cos \beta) - (x_z) \cdot (\sin \beta)] \quad (22)$$

By utilizing Equations (19) and (20), we can determine the angle of the roll axis

$$\tan \alpha = \left(\frac{\sin \alpha}{\cos \alpha} \right) = \left[\frac{-(z_y)}{(z_x) \cdot (\sin \beta) + (z_z) \cdot (\cos \beta)} \right] \quad (23)$$

The angle of the yaw axis for the outermost frame can be represented by Equations (21) and (22) as follows:

$$\tan \gamma = \left(\frac{\sin \gamma}{\cos \gamma} \right) = \left[\frac{-(y_x x_x) \cdot (\cos \beta) + (y_z) \cdot (\sin \beta)}{(x_x) \cdot (\cos \beta) - (x_z) \cdot (\sin \beta)} \right] \quad (24)$$

Applying the arc tangent function to Equations (23) and (24), we obtain

$$\alpha = \tan^{-1} \left[\frac{-(z_y)}{(z_x) \cdot (\sin \beta) + (z_z) \cdot (\cos \beta)} \right] \quad (25)$$

$$\gamma = \tan^{-1} \left[\frac{-(y_x x_x) \cdot (\cos \beta) + (y_z) \cdot (\sin \beta)}{(x_x) \cdot (\cos \beta) - (x_z) \cdot (\sin \beta)} \right] \quad (26)$$

Equations (18), (25), and (26) are utilized to calculate the coordinates of the three rotating axes of the platform. The relationship of the three linear axis coordinates is expressed by Equation (17) as follows:

$$x = (o_x) \quad (27)$$

$$y = (o_y) \quad (28)$$

$$z = (o_z) \quad (29)$$

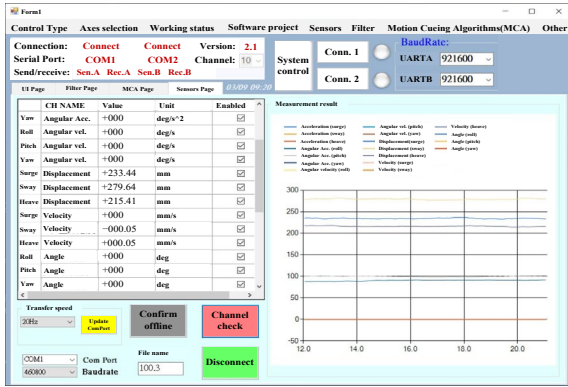
The Equations (18), (25), (26), and (27)–(29) are derived to calculate the six-axis coordinates.

MONITORING SYSTEM

The monitoring system was specifically developed for testing a proposed six degree-of-freedom motion platform. It consists of a human-machine operation module and a PC-based monitoring module, as shown in Figures 3(a) and (b) respectively. The former allows for the selection of control modes. Utilizing a DSP as the control core, it executes motion algorithms to generate sensory effects for trainers. By establishing communication with the PLC controller, the module can enter the simulation mode of the motion platform, indicated by a green box in the DSP communication status. The HMI facilitates the relevant settings and operations for servo multi-axis control. The purpose of this section is to utilize the monitoring module to test the dynamic characteristics of the proposed six-axis motion platform and conduct intrusion tests using six installed photoelectric switches. The latter module primarily consists of a three-axis attitude gyroscope, three long-distance laser displacement sensors, three short-distance laser displacement sensors, three angular velocity sensors, and a three-axis accelerometer. It provides data for testing purposes.



(a)



(b)

Fig. 3 The monitoring module interface: (a) HMI; (b) PC-based monitoring interface.

IMPLEMENTATION

To accommodate the continuous rotation capability of the proposed motion platform, three slip rings are installed. These slip rings are positioned on the inner frame, outer frame, and upper and lower axis sliders. Their purpose is to facilitate the transmission of power and control signals required for the pitch axis, roll axis, and yaw axis, as well as for internal use within the cockpit. Omron's E3Z-T61 model of optoelectronic switches will be used for detection within a distance of 10 meters. Each switch consists of a light emitter and a light receiver, and six sets will be installed at six positions requiring detection.

The proposed electrical control cabinet incorporates a digital processing control board that utilizes Texas Instruments' DSP (TMS320F28377D) in conjunction with Omron's PLC (NJ-501) as the control core of the six-degree-of-freedom platform. It is equipped with a human-machine interface that allows testing through pre-written interface programs, as shown in Figure 4. The power source is provided by the mains and an UPS. The slip ring design allows unlimited rotation for the roll, pitch, and yaw axes. The monitoring computer is used for real-time monitoring, and when the optoelectronic switches detect personnel intrusion or abnormal faults, the actual problems occurring in the system can be immediately traced through established data, statuses, and correlations. The primarily consists of a digital processing control board, a PLC, an HMI, eight servo motors (three of which are mounted on the rotary mechanism), and peripheral modules. It establishes a multi-axis motion control system with digital communication. Additionally, six photoelectric switches are incorporated for safety monitoring of the large-scale

motion platform. Thanks to EtherCAT's capabilities, which include rapid data transmission and the adoption of distributed clock technology for excellent synchronization performance, this system benefits from a distributed daisy-chain topology that eliminates the need for hardware command allocation to each servo group and reduces the command cycle time. EtherCAT is fully compatible with standard networks due to its topology structure and packet format, enabling the encapsulation of commands for various slave stations within a single packet. This enhances network efficiency by allowing the issuance of commands to all slave devices with a single packet. EtherCAT communication ports are used to read and receive relevant commands or sensor signals, as depicted in the figure above. Table 1 presents the relevant parameters of the servo motors used in this study, which are EtherCAT compatible and manufactured by TECO Company.

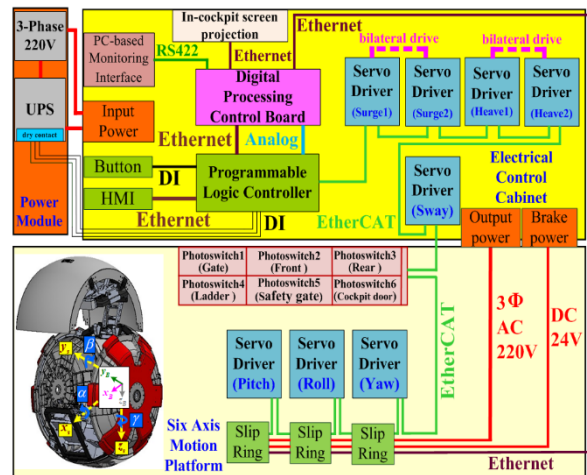


Fig. 4 6-DoF motion control system block.

Table 1 The parameters of the motor.

DoF Item	Surge1 & Surge2	Sway	Heave1 & Heave2	Roll	Pitch	Yaw
Power dissipation (kW)	15	7.5	15	5.5	4.4	7.5
Rated speed (r/min)	1500	1500	1500	1500	1500	1500
Maximum Speed (r/min)	2000	2000	2000	2000	2000	2000
Rated Torque (N.m)	95.5	47.8	95.5	35	28.4	48
Maximum Torque (N.m)	204	122.6	204	87.6	71.1	119
Rotor inertia (kg-cm ²)	235.2	110.88	235.2	92.38	67.83	132.2
Inertia ratio of the proposed	2.5	3.4	1.9	4.8	7	25

system						
Mass of the proposed system (kg)	11,200	4,500	3,200	1,100	440	1,900

The operational mechanism described in this paper utilizes a state machine to manage platform operation states, as illustrated in Figures 5(a) and (b). Fig. 5(a) and (b) depict the execution processes during normal operation and error occurrence, respectively, with detailed state descriptions compiled in Table 2. From the flowchart in Fig. 5(a), it is evident that after the airplane simulator starts, the platform enters the Locked State. At this point, the operator sequentially sends Reset and Active commands to unlock the platform, placing it in the Waiting State. The controller then receives commands from FlightGear to initiate flight training. Upon completion of the training session, Reset or Descend commands are sent to return the cockpit to the boarding ladder position, transitioning the platform to the Resting State, awaiting new instructions. In the event of a Major Failure State or Minor Failure State, as depicted in Fig. 5(b), the platform transitions from the Normal Operating State to the Failure State. At this point, the platform immediately halts and enters the Resetting State, where personnel diagnose the cause of the error and troubleshoot. Once confirmed to be without issues, if it was a Major Failure State, the operator sends the Lock command to return to the Locked State, or if it was a Minor Failure State, the operator sends the Active command to return to the Normal Operating State for simulator training mode.

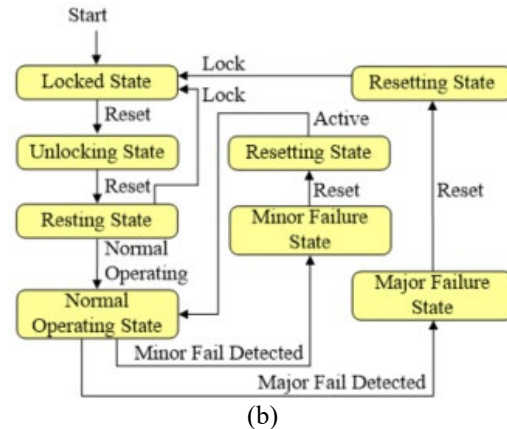
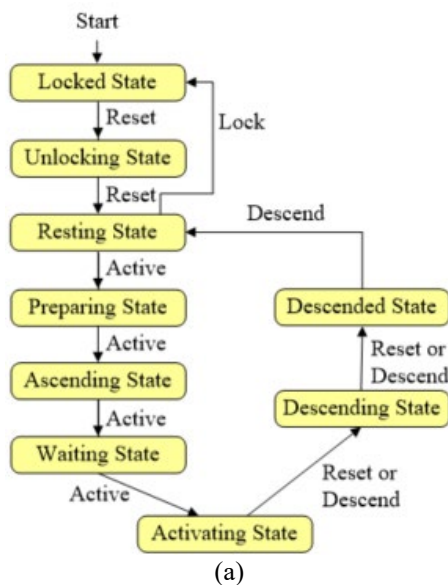


Fig. 5 State machine execution process: (a) state during normal operation; (b) state during error occurrence.

Table 2 State machine details.

Type	Description
Locked State	Platform locked state, only accepts Rest command
Resting State	Platform resting state, does not accept any commands
Major Failure State	Major error state (software limits, hardware limits, emergency switch, and servo-related errors)
Minor Failure State	Minor error state (six photoelectric switches triggered)
Preparing State	Platform parameter initialization state
Ascending State	Platform ascending to center point
Waiting State	Platform reached center position, waiting to start
Activating State	Receiving platform commands for flight training
Descending State	Platform descending to original position
Descended State	Platform returned to original position
Resetting State	Error troubleshooting
Unlocking State	Platform unlocking state

EXPERIMENTAL VALIDATION

Six sets of photoelectric switches are installed at key locations around the platform: the main door, the boarding ladder, the cockpit door, the safety door, the front of the platform, and the rear of the platform, as illustrated in Figures 6(a) to 6(f). Due to the simulator's capability for long travel and large-angle movements, it operates within an independent motion space, allowing trainees to fully concentrate on their flight training. As shown in Figs. 6(a) and 6(d), each door is equipped with a pair of photoelectric switch transmitters and receivers. The light from the transmitter directly reaches the receiver. When someone passes between them and blocks the light, this interruption is sent via EtherCAT to the controller, which then activates protective measures. Additionally, photoelectric switches are installed at the front and rear of the platform to prevent accidental intrusions by visitors. This ensures immediate detection and cessation of simulator operations, as depicted in Figs. 6(e) and 6(f). Before commencing flight training, trainees must enter the cockpit by opening the cockpit door via the boarding ladder. Therefore, as illustrated in Figs. 6(b) and 6(c), photoelectric switches are installed at the boarding ladder and cockpit door to monitor trainee movements. This ensures that the simulator only begins operating once personnel are correctly positioned and ready.

When the control system detects the proximity of personnel during platform operation, it immediately halts the motion. In the event of a power outage, the platform's electromechanical subsystems can continue to operate through an UPS system, providing power to the equipment. Simultaneously, it adjusts the descent of the cockpit module to a position allowing the instructor to enter and exit. The experiment aims to integrate the platform with the photoelectric switches and test the operation when personnel intrude. In the experiment, arc interpolation was performed on axes roll and pitch, as well as axes pitch and yaw, for two-axis (X and Y axes) interpolation, while the other axis (Z axis) adopted linear interpolation, to verify the proposed spiral interpolation function. The PLC controller utilizes Sysmac Studio software (2023) for data tracking to perform trending on variables without the need for any additional programming. As a means of data verification, the data is stored for use in testing, operation, and equipment maintenance. Figures 7(a) and (b) depict the selection of axes roll and pitch for arc interpolation, with the center point coordinates at (130, 0) and end point coordinates at (260, 0), while

executing a spiral motion along the Z-axis with a distance of 500 degree. Figures 8(a) and (b) show the selection of axes pitch and yaw for arc interpolation, with the center point coordinates at (160, 0) and end point coordinates at (0, 0), while executing a spiral motion along the Z-axis with a distance of 100 degree, as shown in the response graph. From Figs. 7(a) and 8(a), it can be observed that for circular arc interpolation, the X and Y axes are respectively selected for the roll and yaw axes, while the pitch and yaw axes are selected. The total arc length to be executed is calculated using the built-in circular positioning control command in the PLC. The Z-axis is chosen for the pitch axis and roll axis. By inputting the starting point coordinates, center point coordinates, ending point coordinates, the clockwise or counterclockwise direction of servo rotation, and the Z-axis movement amount for circular arc interpolation on the X and Y axes, the spiral interpolation effect can be achieved. The effect of motion along the Z-axis is clearly observed from Figs. 7–8.

Figure. 9(a)–(d) demonstrate the use of PLC virtual axis commands to enable Surge1 and Surge2 axes to follow the virtual axis. Setting the velocity loop limit and acceleration/deceleration loop limit for the servo drivers to ± 400 mm/s and ± 4000 mm/s², respectively. Fig. 9(a) represents a movement range of -500 mm to +1500 mm (averaging ± 1000 mm). Fig. 9(b) demonstrates the error between surge1 and surge2, indicating an accuracy of approximately ± 0.04 mm for the dual-driven surge axes. Fig. 9(c) displays the actual speeds of surge1 and surge2 measured during motion, showing a good response in speed tracking. Fig. 9(d) illustrates the acceleration response, showing that the Surge1 and Surge2 axes reach a maximum acceleration of approximately ± 23000 mm/s² from a standstill to startup, then stabilizes to an acceleration of approximately ± 4000 mm/s² after 6.5 seconds of motion.

Figures 10(a)–(c) represent the experimental results for the sway axis. Setting the velocity loop limit and acceleration/deceleration loop limit for the servo driver to ± 400 mm/s and ± 3000 mm/s², respectively. Fig. 10(a) shows a movement range of +400 mm to -400 mm (averaging ± 400 mm). Fig. 10(b) presents the actual velocity of the sway axis measured during motion, demonstrating good speed tracking. Fig. 10(c) displays the acceleration response with a maximum of approximately ± 3200 mm/s².

Figures 11(a)–(d) illustrate the use of PLC virtual axis commands to enable heave1 and heave2 axes to

follow the virtual axis. Setting the velocity loop limit and acceleration/deceleration loop limit for the servo drivers to ± 400 mm/s and ± 4000 mm/s², respectively. Fig. 11(a) represents a movement range of +400 mm to -400 mm (averaging ± 400 mm). Fig. 11(b) demonstrates the error between heave1 and heave2, indicating an accuracy of approximately ± 0.01 mm for the dual-driven heave axes. Fig. 11(c) displays the actual speeds of heave1 and heave2 measured during motion, showing a good response in speed tracking. Fig. 11(d) illustrates the acceleration response with a maximum of approximately ± 8200 mm/s².

Figures 12(a)–(c) demonstrate the experimental results for the roll axis. Setting the velocity loop limit and acceleration/deceleration loop limit for the servo driver to ± 55 degrees/s and ± 55 degrees/s², respectively. Fig. 12(a) represents a movement angle range of 0 degrees to +360 degrees. Fig. 12(b) presents the actual velocity of the roll axis measured during motion, which is ± 55 degrees/s, indicating good speed tracking. Fig. 12(c) displays the acceleration response with a maximum of approximately ± 320 degrees/s².

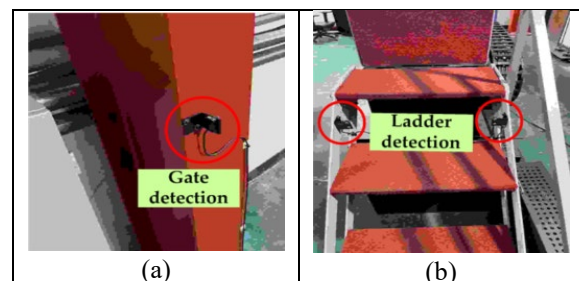
Figures 13(a)–(c) present the experimental results for the Pitch axis. Setting the velocity loop limit and acceleration/deceleration loop limit for the servo driver to ± 100 degrees/s and ± 100 degrees/s², respectively. Fig. 13(a) represents a movement angle range of 0 degrees to +360 degrees. Fig. 13(b) presents the actual velocity of the pitch axis measured during motion, which is ± 100 degrees/s, demonstrating good speed tracking. Fig. 13(c) displays the acceleration response with a maximum of approximately ± 300 degrees/s².

Figures 14(a)–(c) illustrate the experimental results for the yaw axis. Setting the velocity loop limit and acceleration/deceleration loop limit for the servo driver to ± 100 degrees/s and ± 100 degrees/s², respectively. Fig. 14(a) represents a movement angle range of 0 degrees to +360 degrees. Fig. 14(b) presents the actual velocity of the yaw axis measured during motion, which is ± 100 degrees/s. Fig. 14(c) displays the acceleration response with a maximum of approximately ± 300 degrees/s².

In this experiment, test personnel inside the passenger cockpit observed FlightGear visual effects software on screens, as shown in Figures 15(a)–(d). The operator can conduct subject training from a single-seat within the cockpit through a screen. The personnel and the screen have a planned visual focal point of 672mm. The objective of this experiment is to assess the subjects' ability to maneuver the aircraft during taxi on the runway and their response measures

when encountering an intrusion by external personnel during the training process. Fig. 15(a) shows an encounter with personnel intrusion 30 seconds after the training starts, during which the surge axis, sway axis, and heave axis come to a halt at 800mm, 20mm, and 0mm, respectively. As shown in Fig. 15(b), the roll axis, pitch axis, and yaw axis attitudes are approximately -0.1 degrees, 3 degrees, and 1 degree. The platform operates normally immediately when no abnormalities are detected at 35 seconds. Figs. 15(c) and 15(d) represent the relative velocities corresponding to 15(a) and 15(b), respectively. The flight training on the six-axis motion platform is tested using FlightGear as the visual effects software. The tests are conducted using an MTi-680G three-axis attitude gyroscope, three DP-1000G laser displacement sensors, and photoelectric switches. The recorder used is the imc CS 5008 model. Fig. 15(a) shows the results measured using the laser displacement sensors, while Figs. 15(b), 15(c), and 15(d) present the results related to the three-axis attitude gyroscope testing.

Figures 16(a)–(b) display response graphs for the six photoelectric switches under various protective testing configurations. In Fig. 16(a), the platform's position is illustrated, with two black trigger action lines indicating intrusion trigger signals from the front door. Fig. 16(b) showcases the platform's position, again with two black trigger action lines indicating intrusion trigger signals from the front door. During platform operation, upon detection of the initial black trigger action signal, the controller promptly halts all motion and displays an abnormal screen on the touch panel to alert the operator. After the onsite situation is resolved, the second black trigger action signal is received. A comprehensive comparison is presented in Table 3.



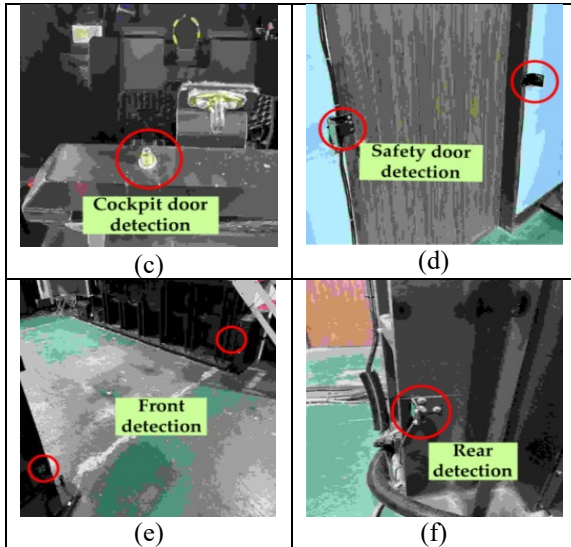


Fig. 6 Installation positions of photoelectric switches: (a) gate personnel intrusion protection; (b) ladder personnel intrusion protection; (c) cockpit door open protection; (d) safety gate personnel intrusion protection; (e) front platform personnel intrusion protection and (f) rear platform personnel intrusion protection.

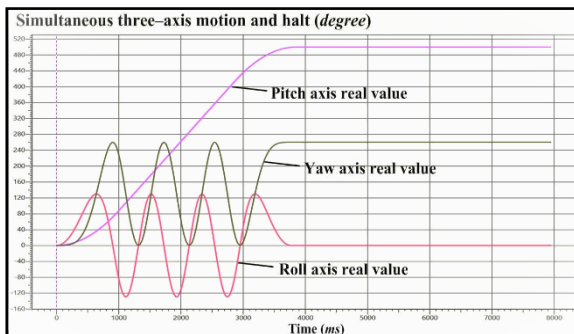
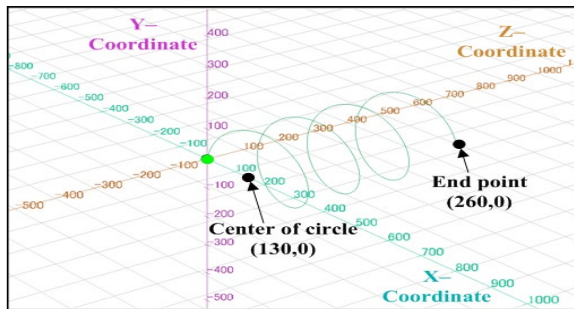


Fig. 7 Measured response of the spiral interpolation for circular motion along the roll and yaw axes, with motion along the z-axis: (a) spiral motion trajectory; (b) three axes of rotation.

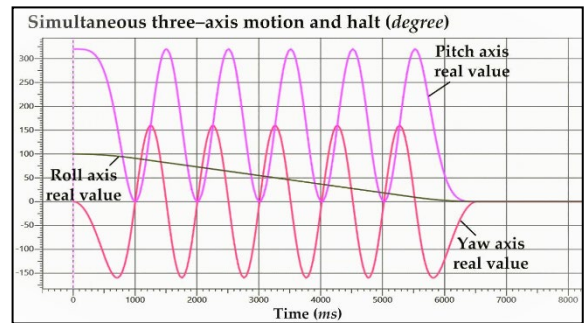
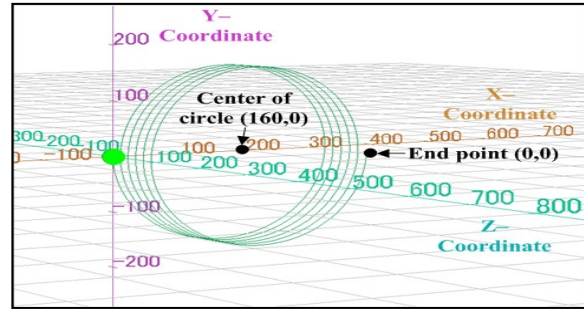
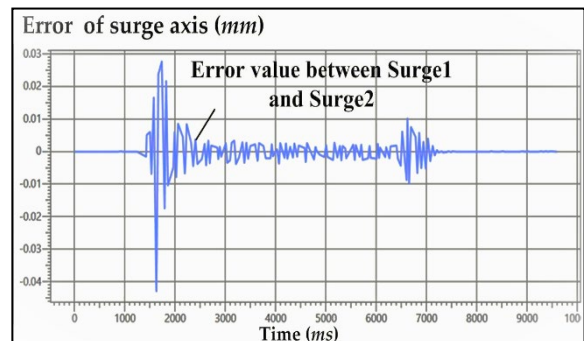
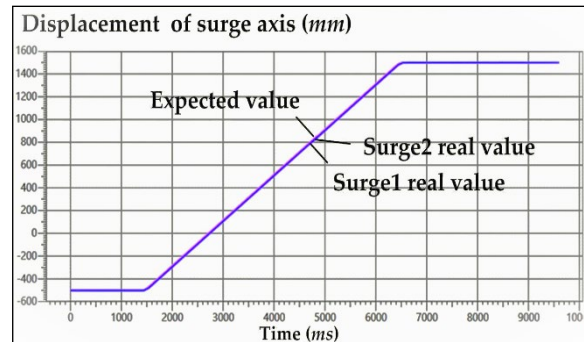
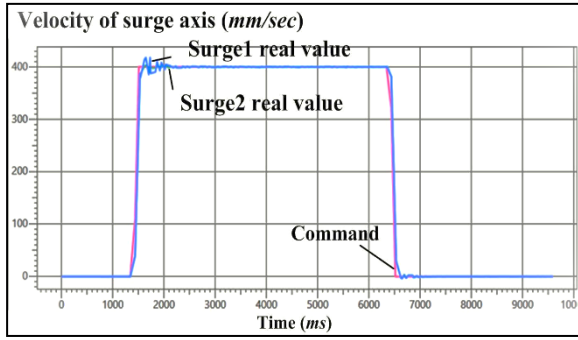


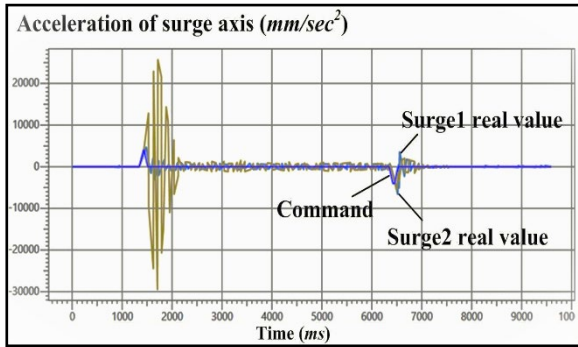
Fig. 8 Measured responses of the spiral interpolation for circular motion along the pitch and yaw axes, with motion along the z-axis: (a) spiral motion trajectory; (b) three axes of rotation.



(b)

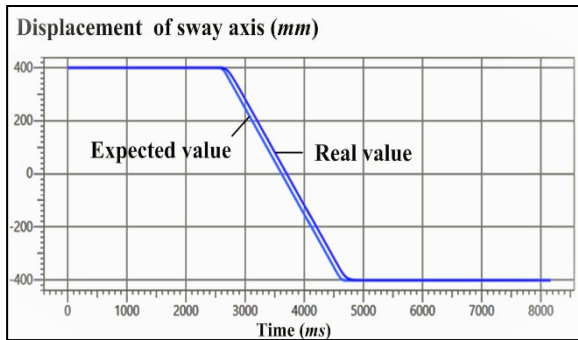


(c)

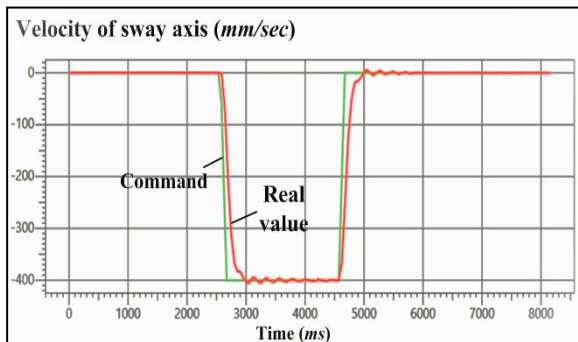


(d)

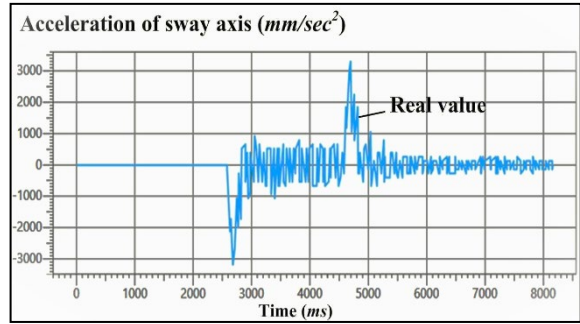
Fig. 9 Measured responses of the surge axis $\pm 1000\text{mm}$ displacement control response diagram: (a) displacement comparison; (b) bilateral drive error value; (c) velocity; (d) acceleration.



(a)

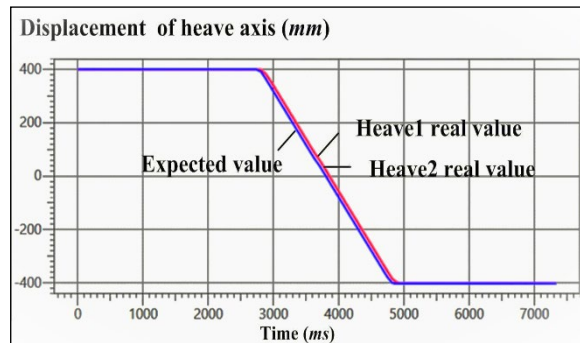


(b)

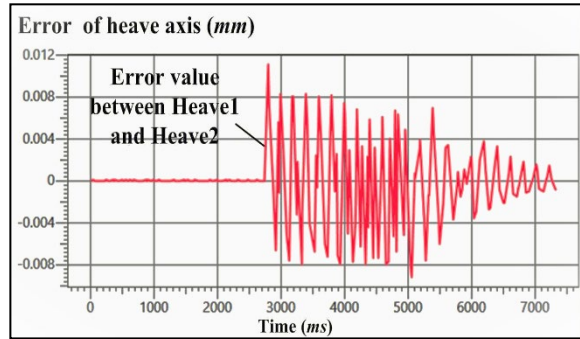


(c)

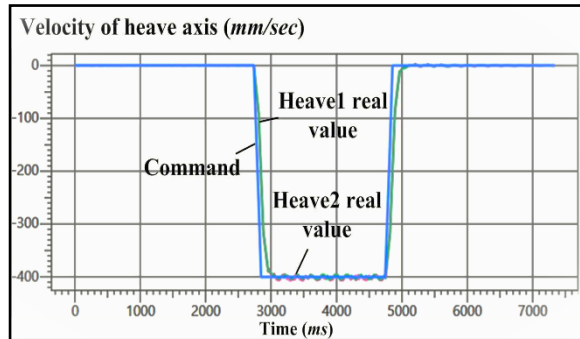
Fig. 10 Measured responses of the sway axis $\pm 4000\text{mm}$ displacement control response diagram: (a) displacement comparison; (b) velocity; (c) acceleration.



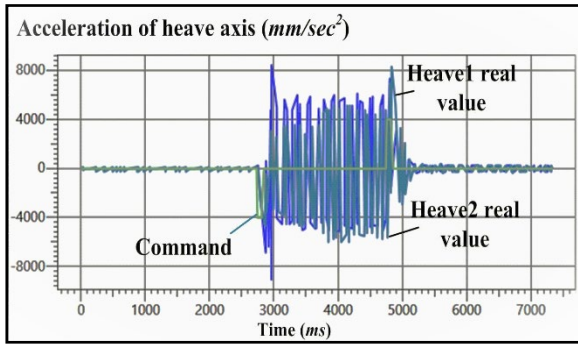
(a)



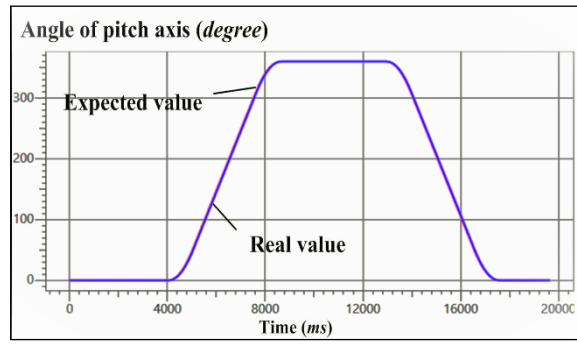
(b)



(c)

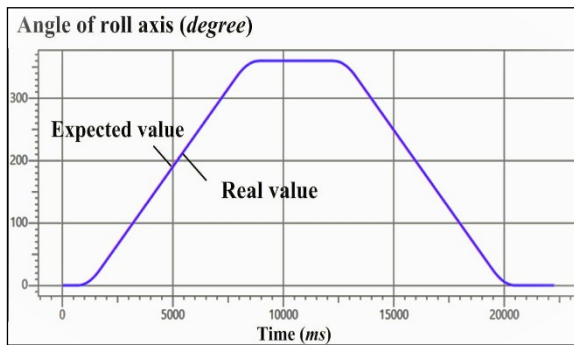


(d)

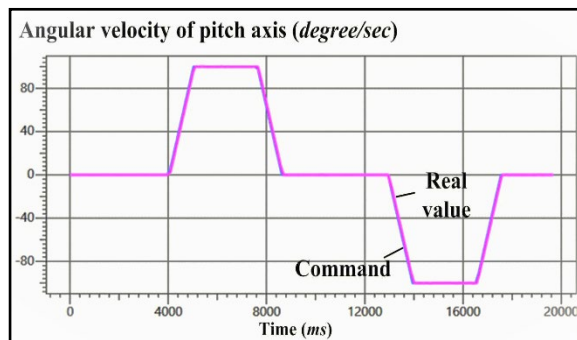


(a)

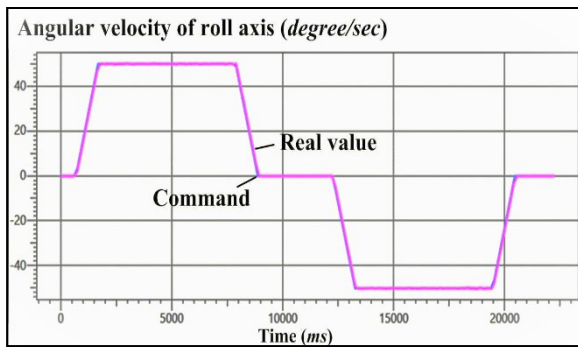
Fig. 11 Measured responses of the heave axis $\pm 400\text{mm}$ displacement control response diagram: (a) displacement comparison; (b) bilateral drive error value; (c) velocity; (d) acceleration.



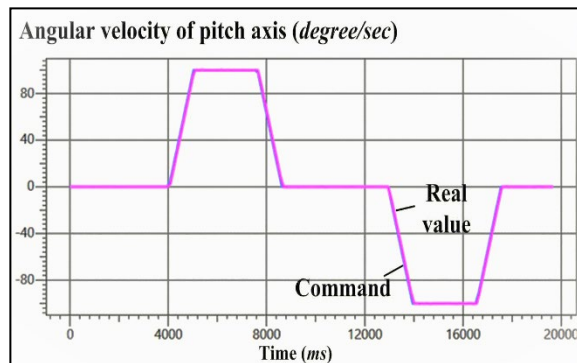
(a)



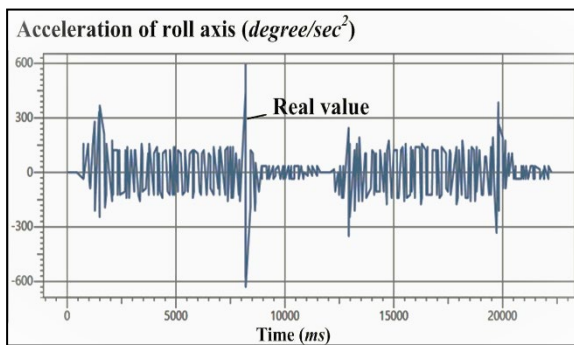
(b)



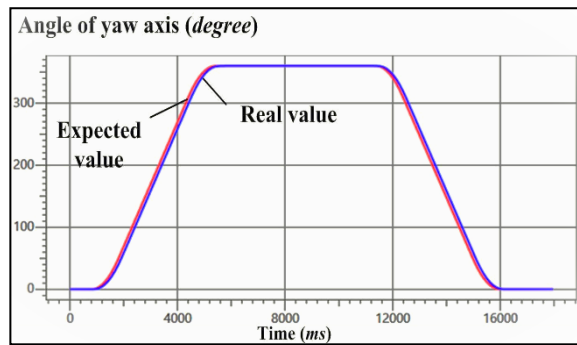
(b)



(c)



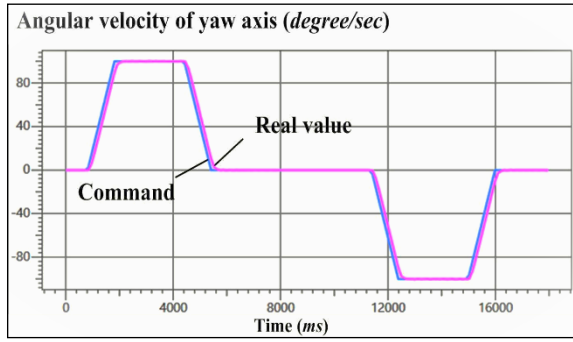
(c)



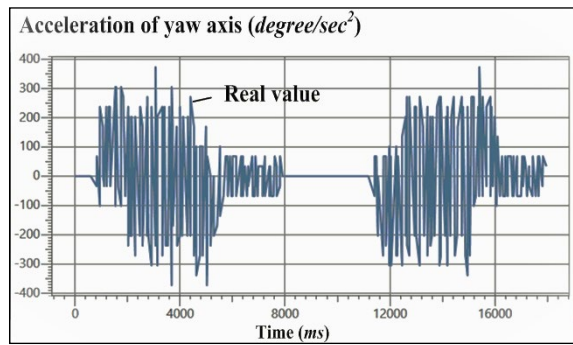
(a)

Fig. 12 Measured responses of the roll axis 0-360 degree: (a) angle; (b) angular velocity; (c) angular acceleration.

Fig. 13 Measured responses of the pitch axis 0-360 degree: (a) angle; (b) angular velocity; (c) angular acceleration.

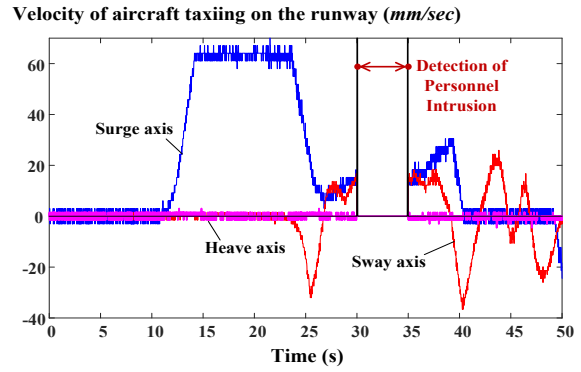


(b)

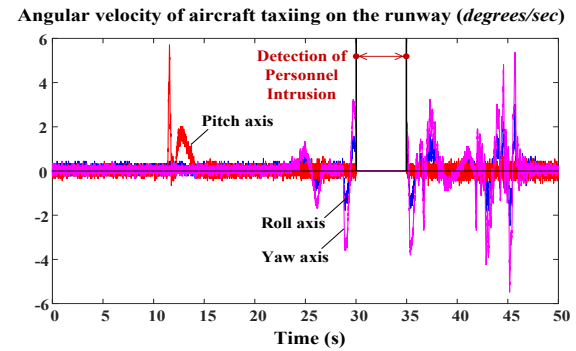


(c)

Fig. 14 Measured responses of the yaw axis 0-360 degree: (a) angle; (b) angular velocity; (c) angular acceleration.

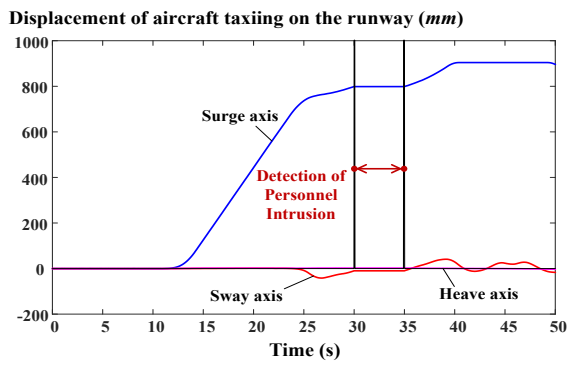


(c)

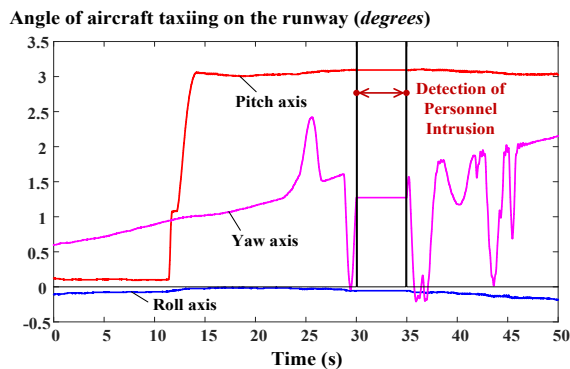


(d)

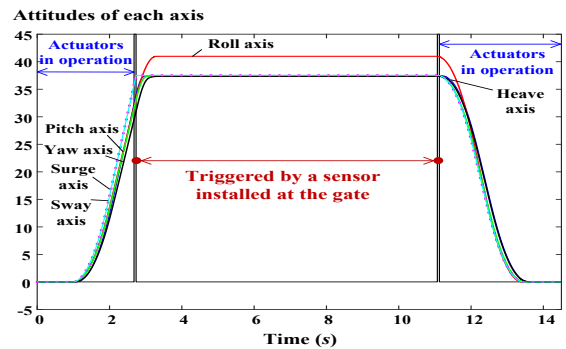
Fig. 15 Measuring responses to personnel intrusion during flight simulator operation: (a) displacement; (b) angle; (c) velocity; (d) angular velocity.



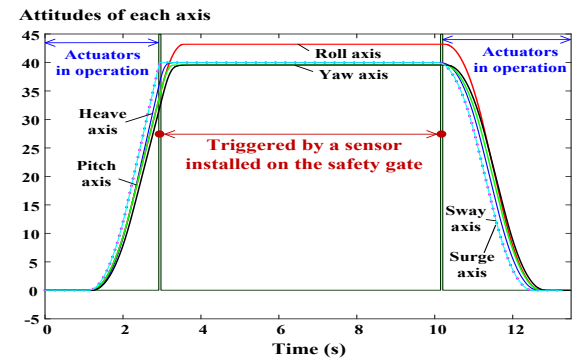
(a)



(b)



(a)



(b)

Fig. 16 Measuring responses from six safety protection devices: (a) gate; (b) safety gate.

Table 3 Comparison of different simulators.

Item DoF	Proposed system	Dancuo et al. (2012)	Emmanuel et al. (2020)
MCA	Yes	No	Yes
Computation time	136 μs	Not provided	> 800 μs
Control architecture	Closed-loop	Closed-loop	Open-loop
Number of axes	Six axes	Three axes	Six axes
Safety measures	The system provides six major safety protection devices.	The system requires assistance from the manufacturer's technician.	The system is not equipped it is a standalone system.

CONCLUSIONS

The proposed multi-axis motion control simulator system represents a significant advancement in simulated aircraft technology. By integrating flight control, servo control, and motion control technologies, the system offers enhanced control protection, simulation realism, and responsiveness. Extensive validation testing with photoelectric switches confirms the system's capability to meet stringent displacement, velocity, and acceleration requirements.

Key performance metrics include:

- 1) Surge motions: Achieving strokes exceeding 2000 mm, velocities over 400 mm/s, and accelerations surpassing 4000 mm/s².
- 2) Sway and Heave motions: Strokes over 800 mm, velocities exceeding 400 mm/s, and accelerations above 3000 mm/s².
- 3) Rotational motions (roll, pitch, yaw): Full 360° rotations, velocities over 50°/s, and accelerations exceeding 100°/s².

These results demonstrate the system's robust performance under diverse operational conditions, showcasing its capability for substantial movements and effective management of rotational dynamics. A crucial aspect of the system is the integration of multi-axis motion control with EtherCAT technology, which facilitates high-speed data transmission with a rate of 5ms. The system operates with a servo drive response frequency of 1ms, ensuring real-time responsiveness and precise control. Additionally, the photoelectric switches employed have a reaction time of 1ms, further enhancing the system's responsiveness and safety measures. The comprehensive HMI and rigorous intrusion testing contribute to the system's precision, reliability, and safety. The proposed system not only meets but exceeds current standards for simulated aircraft technology, offering a high level of operational safety and data transmission efficiency. The combination of advanced technologies ensures that the simulator can effectively replicate the dynamic parameters required for realistic and responsive

aircraft simulations.

ACKNOWLEDGMENT

Financial support for this work was provided by the National Formosa University, Taiwan, under Grant NFU 113-AF-061.

REFERENCES

- Prochazka, F., Krüger, S., Stomberg, G., and Bauer, M. "Development of a hardware-in-the-loop demonstrator for the validation of fault-tolerant control methods for a hybrid UAV," *CEAS Aeronautical Journal*, vol. 12, pp. 549–558, Aug. (2021).
- Wei, M.Y., and Yuan, H.C. "Advanced Servo Control and AI Integration in 3-DoF Platforms for Enhanced Simulation Interactivity," *Appl. Syst. Innov.*, vol. 7, no. 4, pp. 57, Jun. (2024).
- Gough, V.E. "Practical tire research," *SAE Transactions*, vol. 64, pp. 310-318, (1956).
- Stewart, D. "A platform with six degrees of freedom," *Proc. Inst. Mech. Eng.*, vol. 180, no. 15, pp. 371–386, Jun. (1965).
- Wang, S.M. and Ehmann, K.F. "Error model an accuracy analysis of a six-DoF Stewart platform," *ASME Journal of Manufacturing Science and Engineering*, vol. 124, no. 2, pp. 286-295, Apr. (2002).
- Japiong, K.B., Asiamah, G., Owusu-Dabo, E., Donkor, P., Stewart, B., Ebel, B.E. and Mock, C.N. "Availability of resources for emergency care at a second-level hospital in Ghana: A mixed methods assessment," *African Journal of Emergency Medicine*, vol. 6, no. 1, pp. 30-37, Mar. (2016).
- Wei, M.Y. "Design and implementation of inverse kinematics and motion monitoring system for 6DoF platform," *Appl. Sci.*, vol. 11, pp. 9330, Oct. (2021).
- Bi, F., Ma, T., Wang, X., Yang, X. and Lv, Z. "Research on vibration control of seating system platform based on the cubic stewart parallel mechanism," *IEEE Access*, vol. 7, pp. 155637–155649, Nov. (2019).
- Nagata, F., Yoshitake, S., Otsuka, A., Watanabe, K. and Habib, M.K. "Development of cam system based on industrial robotic servo controller without using robot language," *Robot. Comput.- Integr. Manuf.*, vol. 29, no. 2, pp. 454–462, Apr. (2013).
- Wang, C., Zheng, L., Li, B. and Li, Z. "Design and implementation of EtherCAT master based on loongson," *Procedia Computer Science*, vol. 183, no. 2, pp. 462–470, Apr. (2021).
- Ferrari, F.P., Marioli, D., Sisinni, E. and Taroni, A.

- “Wired and wireless sensor networks for industrial applications,” *Microelectron. J.*, vol. 40, no. 9, pp. 1322–1336, Feb. (2009).
- Asadi, H., Lim, C.P., Mohamed, S., Nahavandi, D., and Nahavandi, S. “Increasing motion fidelity in driving simulators using a fuzzy-based washout filter,” *IEEE Trans. Intell. Veh.*, vol. 4, no. 2, pp. 298–308, Jun. (2019).
- Zhao, Q. and Duan, G. “Adaptive finite-time tracking control of 6DoF spacecraft motion with inertia parameter identification,” *IET Control Theory Appl.*, vol. 13, no. 13, pp. 2075–2085, July (2019).
- Qazani, M.R.C., Asadi, H., Khoo, S. and Nahavandi, S. “A linear time-varying model predictive control-based motion cueing algorithm for hexapod simulation-based motion platform,” *IEEE Trans. Syst. Man Cybern. Syst.*, vol. 51, no. 10, pp. 6096–6110, Oct. (2019).
- Asadi, H., Mohamed, S., Lim, C.P. and Nahavandi, S. “Robust optimal motion cueing algorithm based on linear quadratic regular method and a genetic algorithm,” *IEEE Trans. Syst. Man Cybern. Syst.*, vol. 47, no. 2, pp. 238–254, Feb. (2017).
- Barbara, S.M., Marta, G.G. and Marta, M. “Pilots' gaze behavior in simulation research,” *Journal of KONBiN*, vol. 52, no. 4, pp. 1-10, Dec. (2022).
- Golebiewski, M., Galant-Golebiewska, M. and Jasinski, R. “Flight simulator’s energy consumption depending on the conditions of the air operation,” *Energies*, vol. 15, pp. 580, Jan. (2022).
- Berthoz, A., Bles, W., Bühlhoff, H.H. et al. “Motion scaling for high-performance driving simulators,” *IEEE Trans. Hum. Mach. Syst.*, vol. 43, no. 3, 265–276, May (2013).
- Qazani, M.R.C., Asadi, H., Khoo, S. and Nahavandi, S. “A linear time-varying model predictive control-based motion cueing algorithm for hexapod simulation-based motion platform,” *IEEE Trans. Syst. Man Cybern. Syst.*, vol. 51, no. 10, pp. 6096–6110, Oct. (2019).
- Teufel, H.J., Nusseck, H.G., Beykirch, K.A., Butler, J.S., Kerger, M. and Bühlhoff, H.H. “MPI motion simulator: development and analysis of a novel motion simulator,” *In Proceedings of the AIAA Modeling and Simulation Technol. Conf. and Exhibit*, pp. 1–11, (2007).
- Wei, M.Y. “Design of a DSP-based motion-cueing algorithm using the kinematic solution for the 6-DoF motion platform,” *Aerospace*, vol. 9, pp. 203, Apr. (2022).
- Wei, M.Y., Fang, S.A. and Liu, J.W. “Design and Implementation of a new training flight simulator system,” *Sensors*, vol. 22, no. 20, pp. 7933, Oct. (2022).
- NJ-series CPU Unit Software User’s Manual. Available online: [https://www.megatech.ro/doc/606/NJ-series%20CPU%20Unit%20Software%20Users%20Manual%20EN%20\(15%20Mb\).pdf](https://www.megatech.ro/doc/606/NJ-series%20CPU%20Unit%20Software%20Users%20Manual%20EN%20(15%20Mb).pdf) (accessed on 27 December 2023).
- Dancu, Z., Zeljkovic, V., Rasuo, B. and Dapic, M. “High G training profiles in a high performance human centrifuge,” *Sci. Tech. Rev.*, vol. 62, pp. 64–69, (2012).
- Emmanuel, A.M., Luiz, C.S.G. “Identification of the movement algorithm of a commercial platform for helicopter simulators,” *Congresso Brasileiro de Automática-CBA*, vol. 2, pp. 1–8, Dec. (2020).

多軸運動控制在飛行模擬系統中的研製

魏銘彥 蔡文豪

國立虎尾科技大學電機工程系

摘要

這項研究旨在探索多軸運動控制的飛行模擬器系統，重點關注操作安全性和數據傳輸速度。本文提出了機構設計、多軸運動控制和控制系統設計的新概念。所提方法利用飛行、伺服和運動控制技術來加強控制保護、模擬和響應性，從而提升系統性能。系統的有效性通過使用光電開關進行測試得到確認。此外，研究還使用測量系統捕捉動態特性，如行程、速度和加速度。多軸運動控制、數據傳輸、乙太網路控制自動化技術和光電開關的整合增強了模擬器系統中的控制保護和響應性。系統概述強調了座艙的結構組件以及整合六個光電開關以提高數據傳輸速度和安全性。多軸運動控制系統的架構包括基於數位訊號處理器技術的動感演算法和用於伺服運動控制的可編程邏輯控制器。實驗展示了系統對人員入侵和複雜運動的響應，突顯了其安全特性和有效性。這種方法對多軸運動控制系統的領域做出了有價值的貢獻，提高了操作安全性、數據傳輸速度和控制響應性。